Visualizing the Behavior of Dislocations— Seeing Is Believing

Ian M. Robertson, Paulo J. Ferreira, Gerhard Dehm, Robert Hull, and Eric A. Stach

Abstract

The spatial resolution of the transmission electron microscope makes it an ideal environment in which to continuously track the real-time response of a system to an external stimulus and to discover and quantify the rate-limiting fundamental microscopic processes and mechanisms governing the macroscopic properties. Advances in instrumentation, stage design, recording media, computational power, and image manipulation software are providing new opportunities for not only observing the microscopic mechanisms but also measuring concurrently the macroscopic response. In this article, the capability of this technique as applied to mechanical properties of materials is highlighted.

Introduction

By the time transmission electron microscopes (TEMs) began to be used routinely in the 1950s, dislocation theory was at an advanced stage of development and was being applied to disparate fields ranging from crystal growth to deformation processes. The success of the theory was remarkable as it had been developed without dislocations ever having been "seen." This situation changed with the introduction of the TEM and the development of diffraction contrast theories for image interpretation. Since then, TEMs have been used to provide insight into dislocation reactions and interactions and into the dislocation structures produced after processing and deformation. However, the micrographs are "snapshots" in time and provide no information as to the pathway by which the microstructure evolved. With the development of straining stages for use in the TEM, it has become possible to deform a material and continuously track the evolution of the microstructure, and to discover and quantify the rate limiting processes and mechanisms. In this article, examples are given to demonstrate the impact of this technique on our understanding of the mechanical properties of materials, hydrogen embrittlement, dislocation-mediated strain relaxation phenomena in strained-layer epitaxial systems, deformation processes in supported and unsupported thin films, and deformation in nano-sized particles both individually and in aggregate form. In addition, it will be demonstrated that these observations can be used as the foundation for developing physically-based predictive plasticity models that have been used to guide the design and processing of materials.

Specimen Holders for Conducting Dynamic Mechanical Property Tests

To observe dislocation behavior in the TEM requires having a method by which to deform the material. One of the simplest stimuli is the electron beam itself. Thermal stresses associated with local beam heating and the build-up of a surface contamination layer can be sufficient to cause dislocation motion, especially near the electropolished hole where the foil is thinnest.[1] Of course, this method is unreliable, and the dislocation supply is rapidly exhausted. Straining stages that enabled samples to be deformed in a controlled manner were developed in the late 1950s and early 1960s.[2–4] Such stages function by attaching one end of the sample to a moveable rod that runs along the length of the stage body and is connected via a bellows or sliding seal to the external controller.[2] The force to move the sliding rod can be controlled by either a motor or a piezoelectric drive. An example of such a stage and one form of the specimen used are shown in Figure 1. The two holes in the specimen are used to attach it to the stage by means of the mounting pins (labeled p in Figure 1). A clamp is placed over the mounting pins and the sample and secured to the stage via screws (labeled s). These stages, sometimes with the added capability to heat or cool the sample, are responsible for the majority of the work performed to date on dislocation behavior. The limitations of these devices include the inability to measure the applied load and the resultant displacement, because they are displacement-controlled, not load-controlled. An alternate approach, and one that has been used successfully to investigate dislocation processes in supported and unsupported thin films, is to use a heating stage to introduce thermal stresses. The magnitude of these stresses depends on the difference in the thermal expansion coefficients of the sample and the specimen clamping ring or the substrate and can be on the order of several hundred MPa.

Advances in miniaturizing components through microlithographic processes and the development of microelectromechanical technologies have opened new avenues for creating functional devices for use within the limited volume (approximate dimensions 3 mm × 15 mm × 2 mm) available on a TEM sample holder. For example, it is now possible to fabricate miniaturized tensile test frames for use in the TEM.[5,6] The primary advantage of these devices is that they afford the ability to measure the macroscopic properties with μN to nN force resolution while enabling concurrent observation of the responsible deformation mechanisms. The disadvantages of these devices are they are more difficult and costly to
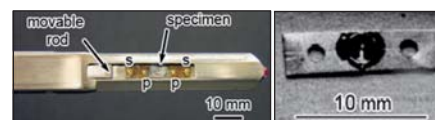

Figure 1. Displacement-controlled straining stage and one possible sample form.

fabricate and the material must be deposited on the substrate, which limits the range of material conditions that can be explored. An example of one of these devices is depicted in Figure 2. In this case, the load is applied using a conventional displacement-controlled stage, and the applied load and strain are determined indirectly by measuring the displacement of the force sensor bar and gauge, respectively. As these devices are recent introductions to the toolkit of electron microscopists, the limitations are only beginning to be revealed and understood. For example, the failure mode of aluminum transitions from ductile shear band[7] to brittle intergranular[8–10] failure as the film thickness decreases below 500 nm; see Figures 2b–2g. For film thicknesses of 200 nm and less, dislocation activity is restricted to a few of the large grains (several hundred nanometers) found along the fracture surface. As the composition of the film shows no significant dependence on film thickness, this transition in failure mode is indicative of a problem. The most likely cause of this transition is grain boundary grooving created during the deposition and fabrication process. The grooves decrease the effective thickness and serve as stress risers, both of which will increase the potential for failure to occur along the grain boundaries. The film thickness dependence on the failure mode is material dependent; gold thin films, for example, fail in a ductile transgranular manner in thickness ranges in which aluminum fails intergranularly.

Other interesting developments in stage design for assessing mechanical properties include the incorporation of a nanoindenter[18–21] or atomic force microscope[11,12] in a TEM holder. The nanoindentation holders, Figure 3, contain a sharp diamond tip that is positioned at the edge of the sample through use of either piezoceramic positioning elements (most common) or nanoscale positioning motors. The diamond is then driven into the sample, and the resulting deformation under the tip is imaged in a cross-sectional geometry.

Before considering applications, a brief discussion of the inherent limitations that arise from using electron transparent samples and a high-energy electron beam is warranted.[2, 13–15] The act of preparing electron transparent samples can alter the
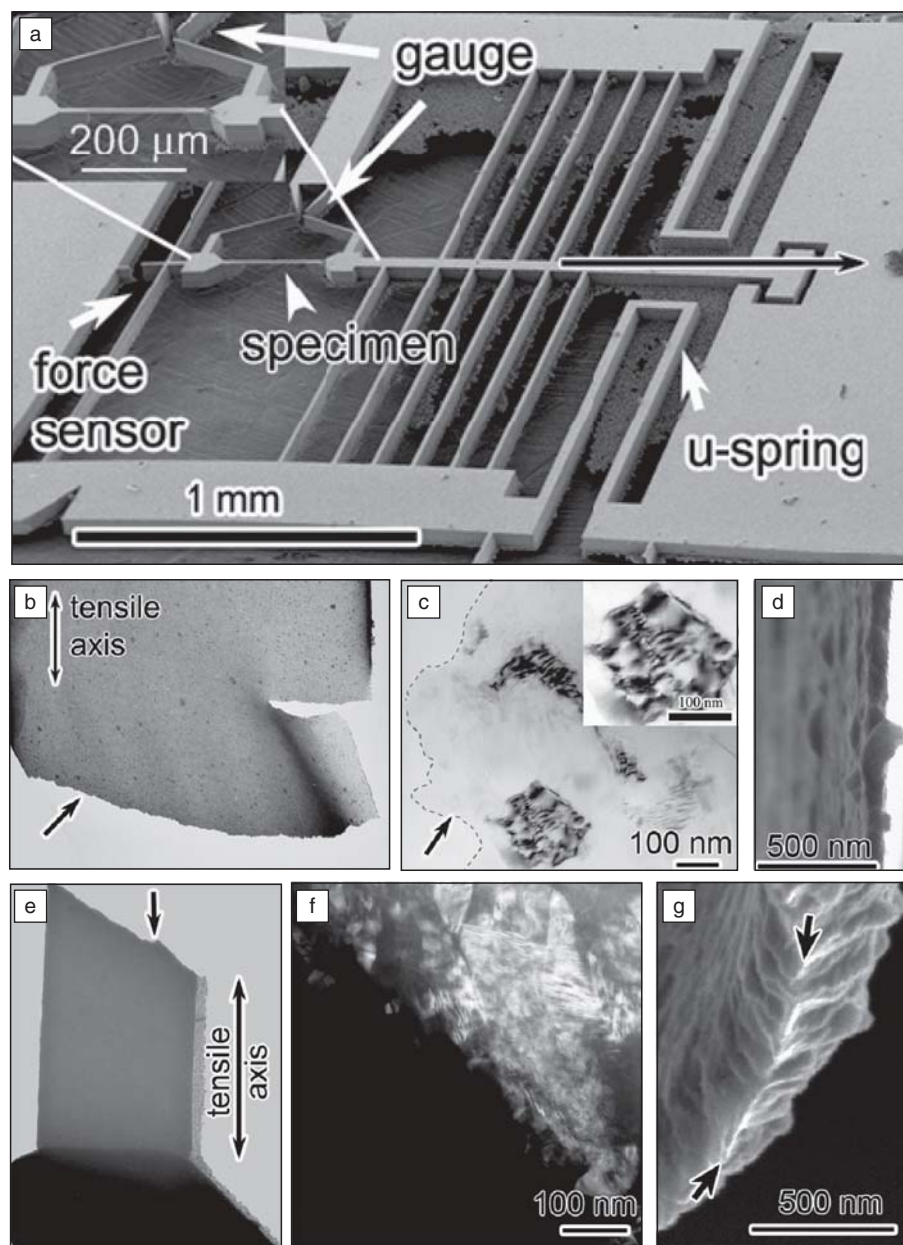
Figure 2. (a) Microfabricated miniature tensile testing frame for free-standing thin films. (b) Failure mode and (c) dislocation structure in isolated grains along the fracture surface, (d) scanning electron microscopy (SEM) image of the fracture surface of 100-nm-thick Al film.[7] (e) Failure mode and (f) dislocation structure in shear band along the fracture surface, and (g) SEM image of the fracture surface of a 500-nm-thick Al film.[105] The dimensions of the gauge sections were 300 μm × 100 μm and 180 μm × 30 μm for the 0.125-μm- and 0.500-μm-thick films, respectively. (Reproduced with permission from Hattar et al, *J. Mater. Res.* **20**:1869. © 2005 Materials Research Society)
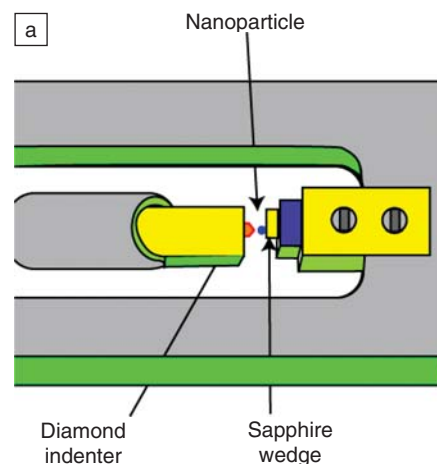
Figure 3. Schematic of a nanoindentation stage.

dislocation structure and cause the relaxation of stresses in strained layer systems. The free surfaces serve as sites for dislocation nucleation and annihilation; surface oxides affect the stress at which dislocations become mobile;[15] and surface image forces alter dislocation configurations and can cause them to be pulled to the surface. Finally, the thickness of the film introduces plane stress conditions. Using a high-energy electron beam to view the specimen can cause an increase in the local temperature; enhance the build-up of a contamination layer; and if the beam energy is above the threshold displacement voltage of the material, vacancies and interstitials are generated. However, provided these limitations are recognized, this technique can be used to follow the evolution of the deformation microstructure, discover the rate-limiting processes, and measure reaction kinetics. In the remainder of this article, examples illustrating application of this technique are provided.

Dislocations and Grain Boundaries

When a crystalline material is deformed in the appropriate temperature range, the permanent or plastic deformation is attributed to the generation, motion, interaction, annihilation, and recovery of dislocations. Initially, it is the preexisting dislocations that are mobile, but additional dislocations must be generated with increasing plastic strain. Possible dislocation sources include pre-existing dislocations, stress concentrators (surface imperfections or cracks), and grain boundaries. An example of the operation of a regenerative dislocation source in molybdenum is shown in the sequence of images presented in Figure 4. In Figure 4a, the source is just completing a cycle and is about to reset. The beginning of the next generative cycle is seen in Figures 4b-4d. In Figure 4d, a dislocation half-loop is seen expanding at a non-uniform rate because of the difference in velocity of edge (labeled e) and screw (s) dislocations in bcc metals. The result is an elongated loop with long straight screw dislocations linked by a short edge segment. In this example, a dislocation loop is not created as the edge segment interacts with the free surface, breaking the link and creating two long straight screw dislocations. The image in Figure 4h captures roughly the same configuration as shown in Figure 4a, but one cycle later. This source will continue to generate dislocations until either dislocations on different slip systems intersect with the expanding half-loop and halt its progression or the local shear stress becomes insufficient.

Although grain boundaries and interfaces serve as sources for generating multiple dislocations,[16–25] they are also effective dislocation sinks. Some grain boundaries can accept and incorporate many dislocations before responding by either cracking or ejecting dislocations. The capacity of the grain boundary to accommodate dislocations and its ultimate response is dependent on the grain boundary misorientation and chemistry, the local stress state, the sample temperature, and the character of the lattice dislocation and how it is incorporated into the boundary. For the case in which dislocation slip is transferred across the grain boundary, the slip system activated by the grain boundary is determined by competition between the local stress condition (applied stress plus dislocation pile-up stress) and minimization of the accumulated strain energy in the grain boundary.[16,26] An example of dislocation accumulation at and accommodation in a random grain boundary in α-Ti as the applied stage displacement is increased is shown in Figure 5. Despite the dislocation density increase in the grain boundary and in the pile-up, the initial response is only an elastic distortion in the adjoining grain, as evidenced by the change in contrast. The grain boundary eventually responds by activating dislocation sources from within the grain boundary.[27] In this case, three slip systems (B, C, and D) are activated (Figure 5c). The dominant slip system was C, with slip systems B and D being secondary. Ejecting dislocations on multiple slip systems was required to minimize the accumulated strain energy. This example illustrates one of the key advantages of the *in situ* technique, namely, the ability to see the dominant processes as well as the order in which they occur—such insight is missing from static snapshots.

The introduction of a nanoindentation TEM stage has provided additional insight into how grain boundaries react to the high applied stresses beneath the indenter tip.[28,29] Observations of nanoindentation of ultra-fine and nano-sized grains have shown that grain boundary motion and stress-driven coarsening are additional relief mechanisms. This is
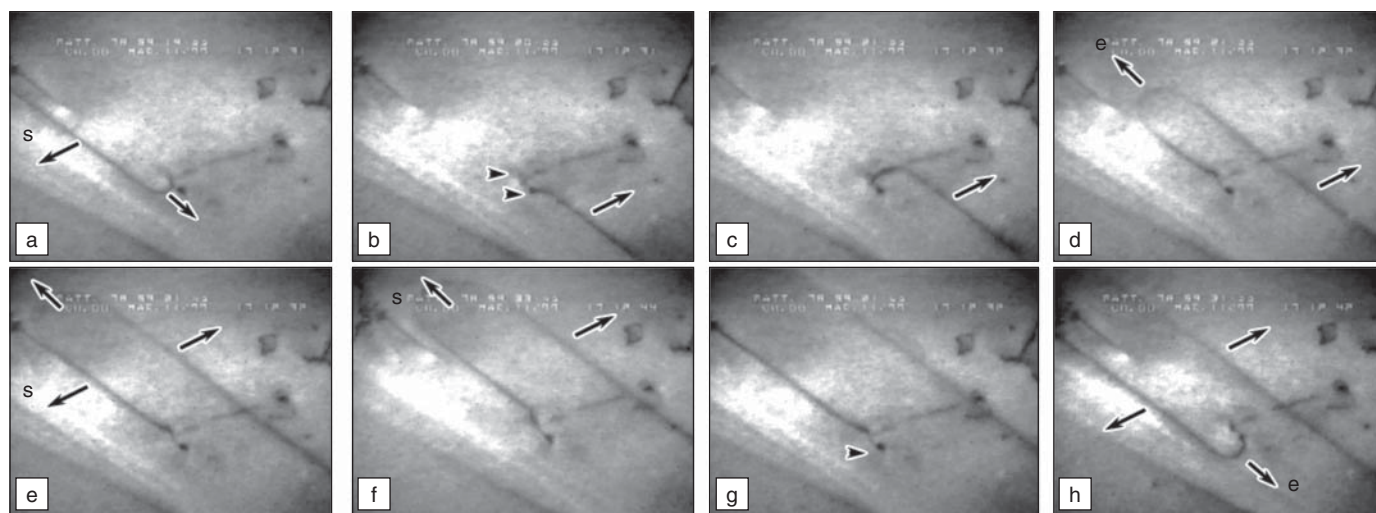

Figure 4. One complete cycle of a dislocation source operating in bcc molybdenum during deformation at room temperature. The arrows indicate the direction of motion of segments of the expanding half-loop; screw segments are labeled *s* and edge components *e*. The arrowheads mark the pinning points.
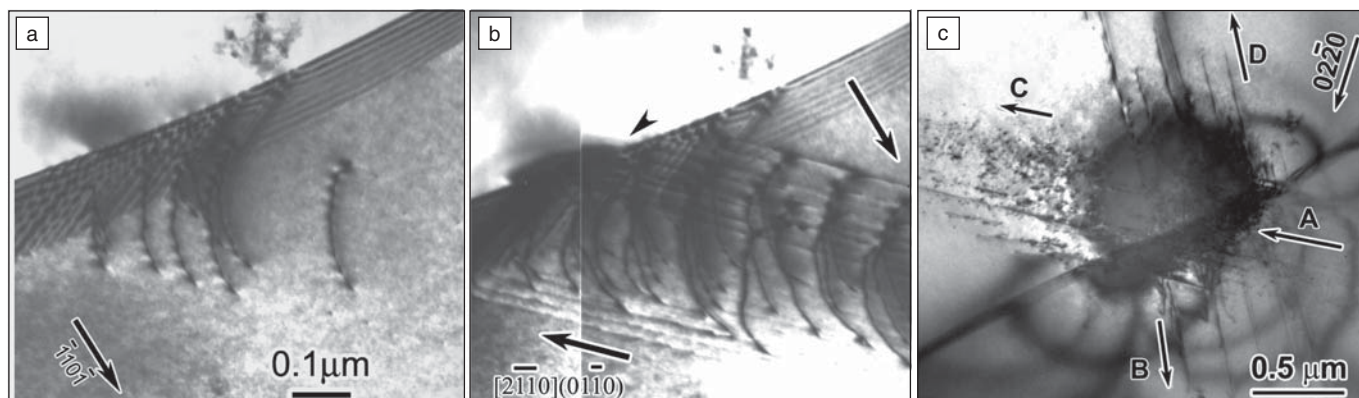
Figure 5. Dislocations interacting with a grain boundary in α-Ti. (a) Initial dislocation structure; (b) dislocation structure after further loading; and (c) eventual response of the grain boundary; the dominant slip system was C; B and D were secondary systems.

illustrated in Figure 6 in which a series of images derived from video-rate observations of the indentation of an aluminum multilayer film is presented. The images show that the grain under load shrinks and the surrounding ones grow as the load increases. This behavior is commonly observed during *in situ* nanoindentation tests and indicates that grain boundary responses in general and grain growth in particular may be important components of the mechanical response of nanocrystalline metals under indentation loading.

One of the challenges of *in situ* investigations, especially when the observations are made in very thin foils, is establishing the relationship between the microscopic processes and macroscopic properties. One success in this regard is in combining quantitative indentation data with real-time images of the indentation process.[30, 31] The load–displacement curve of a nanoindentation experiment conducted in displacement controlled mode is shown in Figure 7a.[32] The images in Figures 7b–7g are still frames extracted from video-rate captures; arrows labeled 1, 2, and 3 connecting pairs of images in Figures 7b–7g correspond to the arrows labeled 1, 2, and 3 in Figure 7a. These show that the onset of plasticity occurs early in the indentation process, even before the establishment of a repulsive contact, and that the steep rise in the load–displacement curve occurs in the presence of a high dislocation density (10^{14} m^{-2}) in the grain. These observations are in stark contrast to prior computational predictions, which concluded that the steep rise was a result of indentation into an otherwise defect-free grain.[33] Instead, it appears that confinement of the dislocations within a single grain can act to significantly strengthen the region being probed.
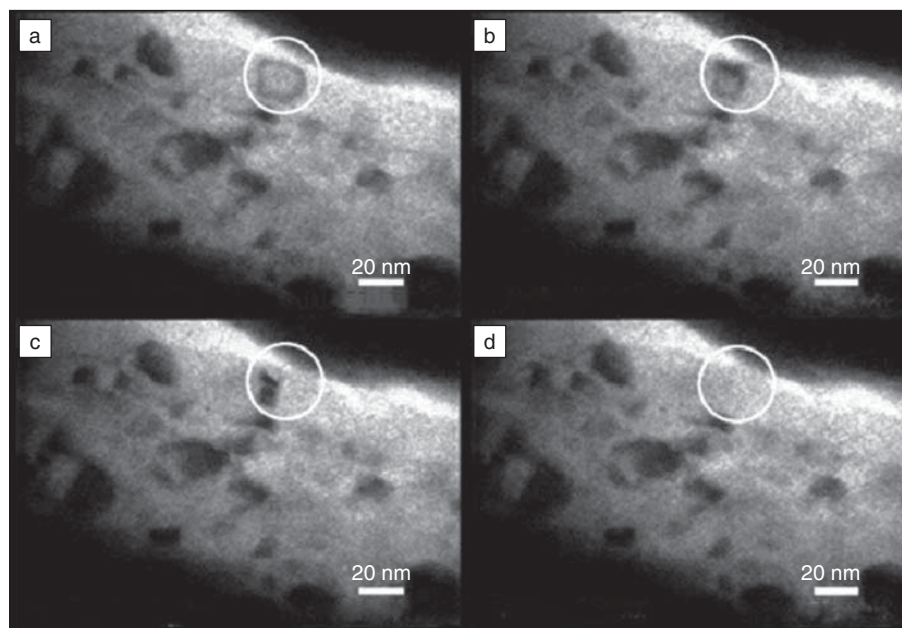

Figure 6. A series of images showing the shrinkage of a nanoscale grain during indentation loading.

The nanoindentation stage has enabled even the response of individual particles under compressive loading to be probed.[32, 34–36] The particles show both elastic and plastic response, and in some cases the particles fracture.[32, 34] Figure 8 shows the changes in contrast of an isolated 35-nm-diameter silver particle during indentation.[36] Although the change in contrast is evident, interpretation remains an issue. The observed contrast changes may be attributed to thickness fringes, bend contours, stress contours, or dislocation activity. Ferreira and coworkers[36] argue that because the particle is permanently deformed (4%) after the indentation, dislocations must have been created and propagated across the particle; they calculated that a total of eight dislocations must have traversed the sample in order to permanently deform the sample by 4%. The absence of dislocations after load release suggests that dislocations in nanoparticles are inherently unstable or that another mechanism such as stress-driven surface diffusion is responsible for the distortion. Additional effort is required to interpret these observations in terms of the deformation processes and the mechanical properties.

Strengthening Mechanisms

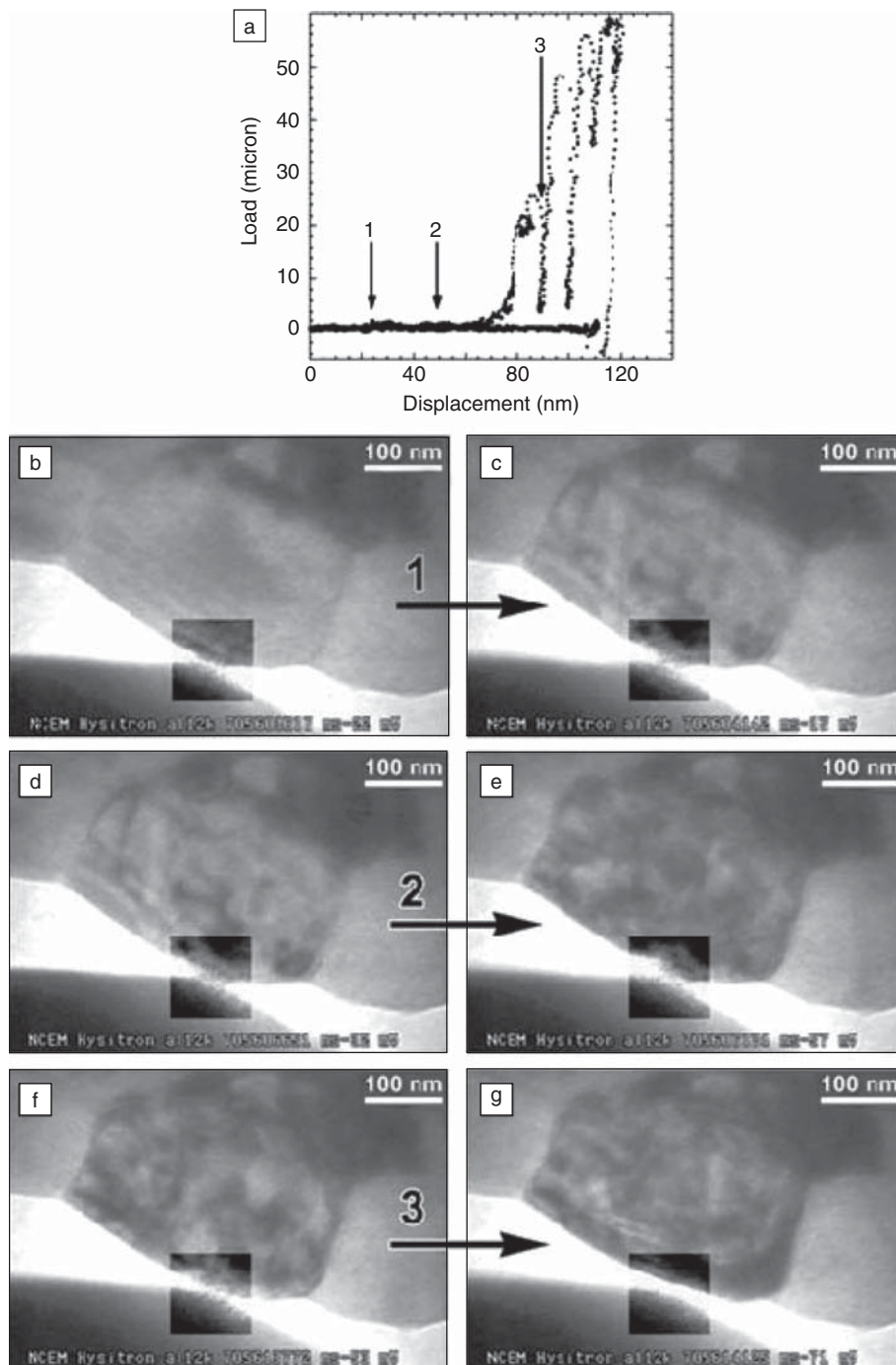To strengthen a metal, obstacles to dislocation motion, such as substitutional

Figure 7. (a) Quantitative load versus displacement curve obtained coincident to an *in situ* nanoindentation test. (b–g) video stills showing the deformation response of the sample at the points arrowed in the load-displacement curve. The image at the point of contact (dark square) has been enhanced to show the contact more clearly.

and interstitial impurities, precipitates, dispersoids (a low-volume-fraction hard phase that is insoluble in the matrix and is added in the melt), dislocations, and grain boundaries and interfaces, are introduced. For precipitate-strengthened systems, the mechanism by which the dislocation bypasses the obstacle depends on the nature of the dislocation (screw or edge type), the size and nature of the precipitate (shearable or non-shearable), the nature of the particle–matrix interface (coherent, partly coherent, and incoherent), the inter-action geometry (the location on the parti-cle at which the slip plane intersects), and the temperature.[37] At room temperature, the possible bypass mechanisms include particle cutting by the dislocation, Orowan looping around the particle, or cross-slip. However, recently it has been established that these simple mechanisms are just a small subset of a myriad of pos-sibilities.[38] With increasing deformation temperature, dislocation climb introduces another degree of freedom by which the dislocations can bypass particles. Again, dislocation dynamics simulations[39] and *in situ* TEM deformation experiments[40] show a range of complex bypass mecha-nisms. An example of dislocations inter-acting with a large, partly coherent, Al_3Sc particle in an Al matrix at elevated tem-perature (nominally 400°C) is shown in Figure 9. The images show that disloca-tions on two slip planes approach the par-ticle from different directions; dislocation 1 approaches the particle from the right and dislocations 2 to 5 from the left. The image contrast shows that the slip planes are different with one steeply (dislocation 1) and the other shallowly (dislocations 2–5) inclined with respect to the foil sur-face. The presence of the second set of dis-locations impacts the interaction of the first dislocation with the particle, even to the extent of forcing it back toward the particle. It is noteworthy that dislocation 1 remains in contact with the particle, whereas four dislocations on the other slip system have interacted with the particle. The changes in the fringe contrast associ-ated with the particles during the interac-tion process suggest that the dislocation is interacting with the particle–matrix inter-face dislocations and it is through this interaction that the bypass process occurs; compare the fringe structure in Figure 9f with that in 9a. This reaction complexity is far from the classical processes on which many of our models are founded.[41–44] The challenge will be to incorporate this new information in future models.

Hydrogen Embrittlement

It is also possible to perform deforma-tion experiments in a gaseous environ-ment inside the TEM.[2, 45] This coupling of stimuli provided the first direct evidence of internal solute hydrogen enhancing the dislocation velocity or the crack propaga-tion rate.[46] The effect was independent of crystal structure and microstructure and occurred in all materials known to be sus-ceptible to hydrogen embrittlement. The generality of the effect inspired the devel-opment of the hydrogen-enhanced local-ized plasticity model of hydrogen embrittlement.[47–50] This model is based on the modification of the dislocation stress

field due to the hydrogen environment that accumulates around it. Simply put, the dislocation-hydrogen complex has a different stress field and consequently experiences different interactions with other elastic obstacles than a dislocation with no atmosphere. In some directions the interaction strength is increased, and in others it is decreased. It is in the directions in which there is a decrease that permits the deformation processes to occur at a lower stress level. Based on these observations, the enhanced plasticity model, as well as the decohesion model, is now accepted as a viable embrittling mechanism. Hydrogen-enhanced plasticity effects are now being incorporated in continuum level models to predict the effect of hydrogen on the bulk mechanical properties of metals.[47–50] This example illustrates how knowledge of fundamental deformation processes can impact the development of continuum level models.

Mechanical Properties of Irradiated Materials

Predicting the mechanical properties of structural materials exposed to the harsh operating environments envisioned for next-generation nuclear reactors presents a major materials challenge.[51] Materials modeling will play a critical role in the development and assessment of candidate material systems. This is a daunting challenge, as we are still trying to understand the complexity of processes that occur in current generation systems. *In situ* electron microscopy coupled with computer simulation has advanced our understanding of how dislocations interact with the irradiation-produced defects.[52–57] For example, Robach et al.[57] showed that the dislocations responsible for creating the defect-free channels observed in bulk deformed materials were freshly generated and not pre-existing ones. Copious numbers of new dislocations were generated from grain boundaries and other stress concentrators and this indicated
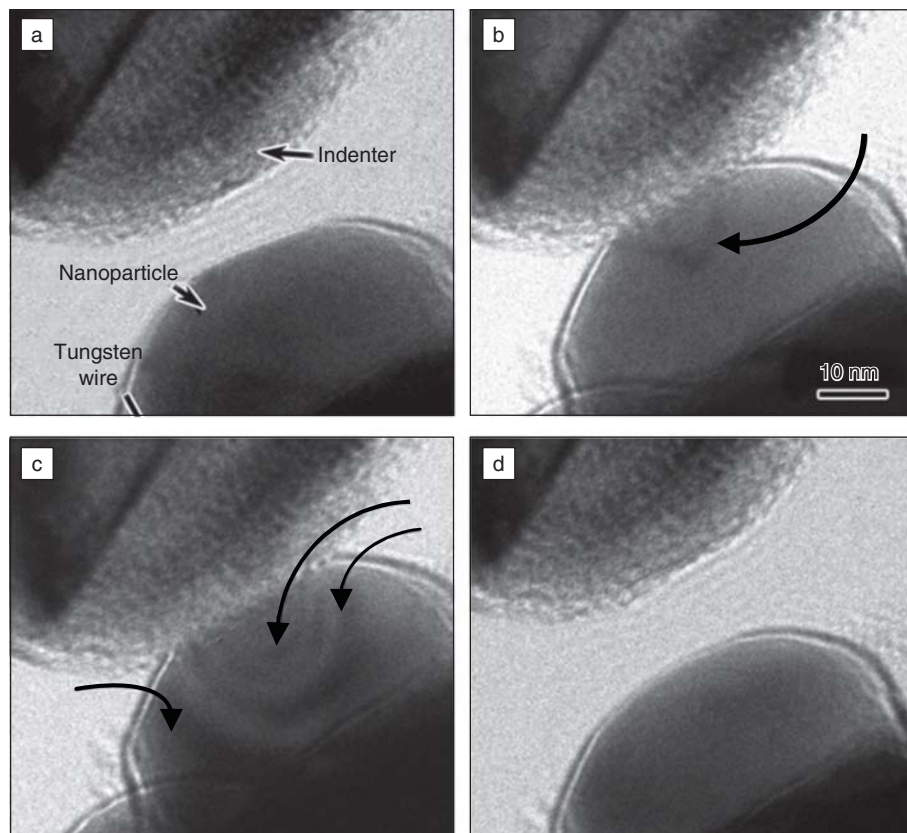

Figure 8. Nanoindentation experiments performed on single Ag nanoparticles. (a) The nanoindentor and the Ag nanoparticle before contact, (b) contact with the Ag nanoparticle, (c) formation of more contrast bands with further loading, and (d) nanoparticle after removal of the nanoindentor.
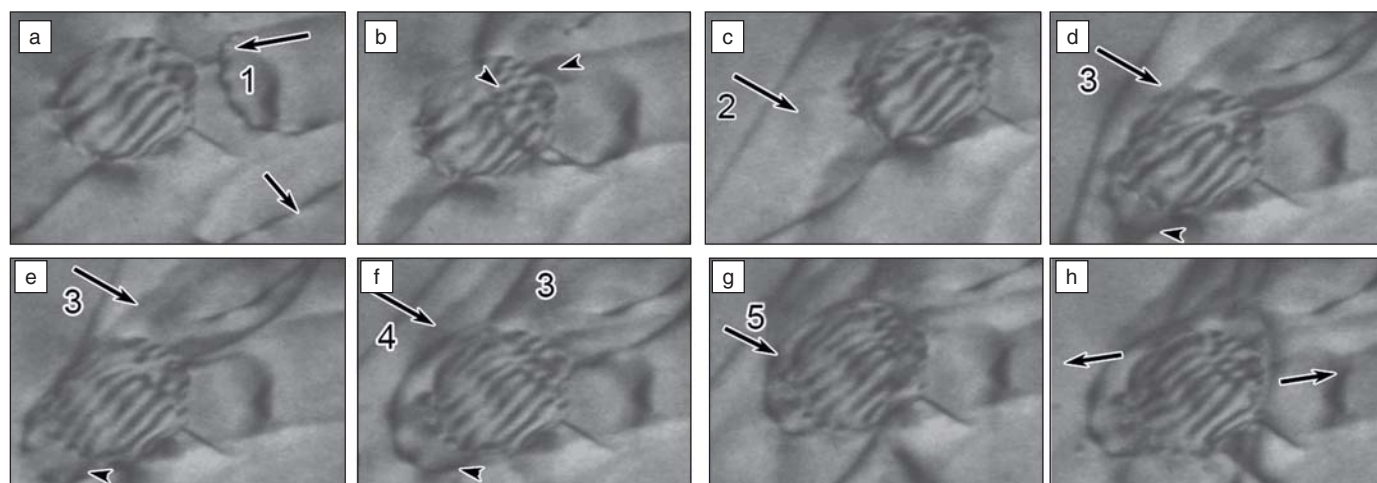

Figure 9. Dislocations interacting with an A1$_3$Sc particle at elevated temperatures. Multiple dislocations of two different slip systems interact with the particle. The interacting dislocations and the direction of motion are indicated. Note the change in the fringe pattern in the particle as the dislocations interact with it.

that the rate-controlling factor was dislocation propagation and not nucleation. Multiple dislocation interactions with an individual obstacle were needed to annihilate the obstacle and the strength of the obstacle as a barrier to dislocation propagation was variable and dependent on its size, the nature of the dislocation, and the geometry of the interaction. Such results contradict all previous assumptions (preexisting dislocations act as regenerative sources, one interaction results in defect annihilation, and each defect has a single strength) that served as the basis for the models.[58–60] This new understanding is forming the basis for the development of continuum models that now show the right form of degradation in the mechanical behavior of irradiated materials.[61]

Strain Relief Mechanisms in Heteroepitaxy

In growing epitaxial films, the set of available materials combinations is greatly expanded if the constraint of lattice matching is relaxed. This leads to the concept of strained-layer epitaxy where different constituent films have different lattice parameters generating a biaxial stress/strain within the deposited films. For the relatively high elastic constants of most semiconductor materials, this gives rise to extremely high stresses and strain energy densities. For example, the lattice mismatch strain for Ge films grown on Si is ~0.041 and the shear modulus is ~60 GPa, giving a biaxial stress of ~10 GPa and a strain energy density of ~10^{11} J m^{-3}. Such large stresses and strain energy densities necessarily give rise to a number of strain relaxation mechanisms, including formation of strain relieving dislocations at the interface between the two materials, morphological instabilities, and surface clustering. In general, these mechanisms are deleterious to device performance (e.g., the interfacial dislocation density affects the diode leakage current).[62] Dislocations create regions of high local carrier generation/recombination, and planar layers are required for most "conventional" device structures. On the other hand, clustered growth can lead to the concept of semiconductor quantum dots, where each cluster can serve as a host for individual carrier charge or spin, giving rise to a host of new potential nanoelectronic device concepts.

In situ transmission electron microscopy has proved to be a valuable tool in developing qualitative and quantitative descriptions of dislocation-mediated strain relaxation phenomena in these systems. By growing epitaxial structures at relatively low growth temperatures, the kinetics of dislocation nucleation and propagation can be suppressed, especially in semiconductors, and structures grown in a metastably strained state.[63] These structures can be subsequently annealed in the TEM, and the processes of misfit dislocation nucleation, propagation, and interaction observed in real time.[64–67] Figure 10 shows a universal curve for misfit dislocation propagation velocities in Si/Ge$_x$Si$_{1-x}$/Si heterostructures, spanning Ge fractions from x = 0.1 to x = 0.4 (with resultant strain ε = 0.041x), Ge$_x$Si$_{1-x}$ layer thicknesses h ~ 10–100 nm, and annealing temperatures T ~ 400–750°C. Data from multiple different structures and experiments are collapsed onto a universal curve according to the relationship:

$$v/\sigma_{ex} = v_0 \exp[-E_v(x)/kT] \qquad (1)$$

Here, v is the measured dislocation velocity; v_0 is an experimentally determined prefactor; $E_v(x)$ is a composition-dependent activation energy for dislocation glide in Ge$_x$Si$_{1-x}$, which from linear interpolation measurements of dislocation glide velocity in bulk Si and Ge (e.g., Reference 68) yields $E_v(x) = 2.2 - 0.6x$ eV; σ_{ex} is an effective or driving stress comprising the difference between the resolved lattice mismatch stress and the dislocation line tension;[90] k is Boltzmann's constant; and T is temperature.[69] Such *in situ* dislocation velocity measurements have also provided insight into dislocation kink (the atomic scale perturbations by which dislocations propagate in materials that have strong inter-atomic bonding) energetics and dynamics.[70–72] *In situ* high-resolution TEM measurements of dislocations in Si[94] and Ge[73] have also provided substantial insight into kink mechanisms. For example, the work of Kolar et al. uses prestressed Si samples to generate built-in kink densities on the partial dislocations.[74] These are imaged in the TEM using the a reflection that occurs only in the stacking fault region between the bounding partial dislocations (Figure 11). Kink migration velocities were measured directly from video imaging during heating *in situ* in the TEM, and kink nucleation energies were determined from the observed kink densities on the two partial dislocations.

To the first order, the strain relaxation rate, ε′, in the sample is proportional to the dislocation velocity, v, through the Orowan equation[75]

$$\varepsilon' = \rho_m b v \qquad (2)$$

Here b is the magnitude of the dislocation Burgers vector, and ρ_m is the mobile dislocation density, which depends on the dislocation nucleation rate. This has been
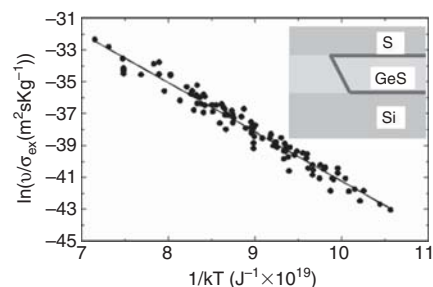

Figure 10. Universal curves of dislocation velocity in the Si/Ge$_x$Si$_{1-x}$/Si(100) system normalized from multiple samples. The magnitudes of the normalized velocities for each measurement point correspond to an equivalent velocity in pure Si at a driving stress of 1 Pa. Inset shows the geometry of the propagating misfit dislocations (dark line).
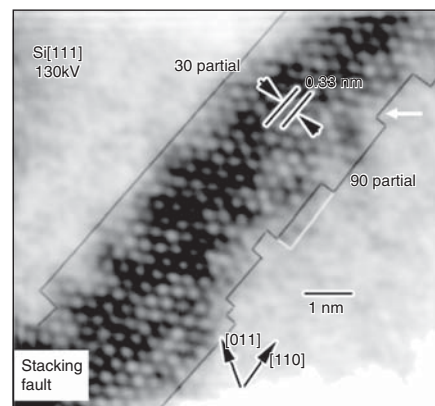

Figure 11. Direct high-resolution imaging of kinks (example indicated with white arrow) on dissociated partial dislocations in Si using the bulk-forbidden a/3422 reflections (Reproduced with permission from Kolar et al, *Phys. Rev. Lett.* 77, 4031, © 1996 American Physical Society)

measured by *in situ* TEM [64, 65] and other methods.[76, 77] A final key process in determining the overall rate of plastic relaxation is the nature of dislocation interactions in these structures. Again, *in situ* TEM has illuminated how dislocation interaction stresses can impede the overall strain relaxation rate,[78, 79] coupling with detailed elastic models of this process[80, 81, 101,102] providing additional necessary input to predictive simulations of the plastic relaxation process.[66, 82]

Similar to semiconductor systems, metallic films with thicknesses in the micrometer and submicrometer range can be grown on substrates and subjected to significant strain during processing and service. As a consequence, irreversible

microstructural changes, delamination, or fracture may occur.[42, 83–88] This failure limits the application of metallic thin films in devices, such as conductor lines in microelectronic or flexible electronic devices or as components in microelectromechanical systems and sensors. Whereas quantitative assessment of thermal stresses are mainly performed by x-ray diffraction, substrate curvature techniques, and/or tensile testing,[89–91] *in situ* TEM is required to shed light on the underlying deformation mechanisms. Especially, a detailed understanding of dislocation nucleation and motion in the films constrained by a substrate and possibly by a surface passivation layer is a prerequisite to explain the mechanical response of metallic thin-film systems.

Most *in situ* TEM studies have been devoted to thermal straining experiments of Al, Cu, Ag, and Au films. Experiments using single-crystal Al and Cu films on α-Al$_2$O$_3$ substrates revealed that dislocations channel through the films and deposit interfacial dislocation segments near the substrate.[92–94] This mechanism is very similar to the formation of lattice misfit dislocations in epitaxial semiconductor films above the critical film thickness, except now the driving force stems from the difference in thermal expansion coefficients between film and substrate. The dislocation channelling mechanism explains an increase in flow stress with decreasing film thickness. Although this is satisfactory for single crystals,[92] it significantly underestimates the stresses in polycrystalline metallic films.[42] *In situ* TEM experiments demonstrated that for polycrystalline metal films on substrates, the film/substrate interface acts as a sink for dislocations and prevents the formation of interfacial dislocation segments.[95] Whereas this in principle lowers the stresses required to move dislocations on inclined glide planes through the film, higher flow stresses are observed for polycrystalline films compared to their single crystal counterparts. This contradiction indicates that in polycrystalline films the rate limiting step is nucleation and not propagation of dislocations.[96] For polycrystalline films, dislocation emission is mostly observed from grain boundary sources, however, the dislocation density decreases with the columnar grain diameter despite the increase in grain boundary density (see Figure 12). *In situ* TEM revealed that for a 100-nm-thick Al film the dislocations emitted from a grain boundary get quickly lost at the film surface,[97] whereas for thicker films cross-slip events are observed that, in turn, increase the probability of the formation of Frank-Read dislocation sources

inside the grains. As a consequence, more dislocation sources are operative in thicker films. It is the local stress associated with dislocation pile-ups acting on the dislocation source that accounts for the higher strength. However, thermal excursions give rise to diffusional processes, which may result in the formation of hillocks[98,119] or cause local stress inhomogeneities.[99] One prominent example discovered by *in situ* TEM is the formation of dislocations emitted as a result of surface and grain boundary diffusion on glide planes, which should not be active according to the global stress state.[100] These dislocations are termed parallel glide dislocations since they travelled on (111) planes parallel to the interface between the film and the substrate.[100] The parallel glide dislocations reveal the interaction of diffusion and dislocation plasticity for strain relaxation.

In contrast to metallic films on stiff substrates, where deformation is induced by thermal straining, tensile straining is the deformation mode for free-standing metal

films[9, 88] or metal films on flexible substrates.[101] Recently, straining of single-crystal Au films on polyimide revealed a transition from perfect to partial dislocation glide with decreasing film thickness.[102] The glide of Shockley partial dislocations was first noticed in an 80-nm-thick Au film and became the dominant deformation mechanism in a 40-nm-thick film (Figure 13). This corresponds to the transition from perfect dislocation glide to twinning as reported for nanocrystalline bulk metals.[103] The transition is size-dependent, as below a certain thickness the nucleation barrier for perfect dislocations exceeds the critical nucleation stress required to form partial dislocations and the corresponding stacking fault.[104]

These changes in deformation mechanisms may become crucial in understanding some of the unexpected mechanical properties of novel nanostructured materials with microstructural features and/or dimensions in the nanometer regime. In the future, a close link between simulation
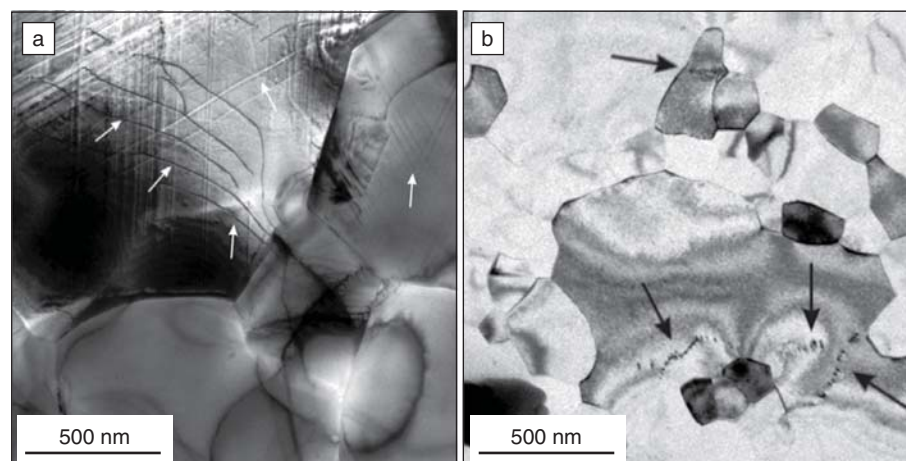
Figure 12. Comparison of dislocation activity in a 600-nm- and a 50-nm-thick Al film on a silicon substrate. [89] (Reproduced with permission from Eiper et al, *Acta Mater.*, **55**:1941.© 2007 Elsevier)

Figure 13. Video frame images showing the glide of partial dislocations. (a) Before and (b) after the glide of a leading partial dislocation that was emitted from the twin *aa'* (the white arrow). The stacking fault was left behind the partial dislocation. (c) A few seconds after the first partial (in this case, 8.5 s), the trailing partial was emitted and swept out the stacking fault. Then, the partials recombined to a perfect dislocation which cross-slipped into the twin *bb'*.[102] All three micrographs were taken at same scale. (Reproduced with permission from Oh et al, *Acta Mater.* **55**:5558 © 2007 Elsevier)

(of plasticity) and *in situ* electron microscopy will be vital for implementing the next generation of advanced materials.

Summary

The ability to "see" how dislocations respond to an external stimulus provides unique insight regarding how dislocation reactions and interactions, either individually or cooperatively, control macroscale properties. The insight garnered from such studies can provide a physical basis from which to develop models to predict properties; such advancements will accelerate the development and property assessment of new materials that are required to enable numerous technological advances. The advances in electron microscopes, recording equipment, and computational tools, and in our ability to create high functionality devices that can be used in electron microscopes provide a unique opportunity to correlate fundamental microscopic processes with macroscopic responses. We are just beginning to appreciate the complexity of dislocations reactions and interactions and how they relate to macroscopic properties.

References

1. P.B. Hirsch, R.W. Horne, and M.J. Whelan, *Phil. Mag. A* **1**, 677 (1956).
2. E.P. Butler, *Reports Prog. Phys.* **42**, 833 (1979).
3. H.G.F. Wilsdorf, *ASTM Spec. Tech.* **245,** 43 (1958).
4. U. Messerschmidt and F. Appel, *Ultramicroscopy* **1**, 223 (1976).
5. M.A. Haque and M T.A. Saif, *J. Microelectromechanical Syst.* **10**,146 (2001).
6. Y. Zhu and H.D. Espinosa, *Proc. Nat. Acad. Sci.* **102**,14503 (2005).
7. K. Hattar, J. Han, M.T.A. Saif, and I.M. Robertson, *J. Mater. Res.* **20**, 1869 (2005).
8. M.A. Haque and M.T.A. Saif, *Scripta Mater.* **47**, 863 (2002).
9. M.A. Haque and M.T.A. Saif, *Proc. Nat. Acad. Sci.* **101**, 6335 (2004).
10. L. Rajagopalan, J.H. Han, and M.T.A. Saif, *Science* **315**, 1831 (2007).
11. D. Golberg, P.M. F.J. Costa, O. Lourie, M. Mitome, X. Bai, K. Kurashima, C. Zhi, C. Tang, and Y. Bando, *Nano Letters* **7**, 2146 (2007).
12. D. Golberg, X.D. Bai, M. Mitome, C.C. Tang, C.Y. Zhi, and Y. Bando, *Acta Mater.* **55**, 1293 (2007).
13. T. Imura, *High Voltage Electron Microscopy,* P.R. Swann, M.J. Goringe, and C.J. Humphreys, Eds., 179 (London, Academic, 1974).
14. H. Saka and T. Imura, *J. Phys. Soc. Japan* **32**, 702 (1972).
15. M.H. Loretto. *Observation and Characterisation of Dislocations. Dislocations and Properties of Real Materials* **323,** 15 (London, The Institute of Metals, 1985).
16. T.C. Lee, I.M. Robertson, and H.K. Birnbaum, *Acta Metall. et Mater.* **40**, 2569 (1992).
17. M. Benyoucef, A. Coujou, B. Barbker, and N. Clement, *Mater. Sci. Eng. A* **234–236**,692 (1997).
18. S. Zghal, A. Coujou, and A. Couret, *Diffusion and Defect Data Pt. B* **59–60**,165 (1998).
19. L.M. Hsiung, A.J. Schwartz, and T.G. Nieh, *Scripta Mater.* **36**,1017 (1997).
20. D. Haeussler, U. Messerschmidt, M. Bartsch, F. Appel, and R. Wagner, *Mater. Sci. & Engin. A* **233**, 15 (1997).
21. B. Baufeld, D. Baither, U. Messerschmidt, and M. Bartsch, *Phys. Stat. Sol. (A)* **150**, 297 (1995).
22. J. Gemperlova, A. Jacques, A. Gemperle, and N. Zarubova. *Interface Science* **10**, 51 (2002).
23. W.A.T. Clark, C.E. Wise, Z. Shen, and R.H. Wagoner, *Ultramicroscopy* **30**, 76 (1989).
24. X. Baillin, J. Pelissier, A. Jacques, and A. George, *Phil. Mag. A* **61**, 329 (1990).
25. F.K. LeGoues, M.C. Reuter, J. Tersoff, M. Hammar, and R.M. Tromp, *Phys. Rev. Lett.* **73**, 300 (1994).
26. T.C. Lee, I.M. Robertson, and H.K. Birnbaum, *Metall. Trans. A* **21**, 2437 (1990).
27. J. Shirokofff and I.M. Robertson, unpublished work.
28. M. Jin, A.M. Minor, E.A. Stach, and J.W. Morris, Jr., *Acta Mater.* **52**, 5381 (2004).
29. M. Jin, A.M. Minor, and J.W. Morris Jr., *Thin Solid Films* **515**, 3202 (2007).
30. W.W. Gerberich, W.M. Mook, M.D. Chambers, M.J. Cordill, C.R. Perrey, C.B. Carter, R.E. Miller, W.A. Curtin, R. Mukherjee, and S.L. Girshick, *Trans ASME. J. Appl. Mechs.* **73**, 327 (2006).
31. A.M. Minor, S.A.S. Asif, Z.W. Shan, E.A. Stach, E. Cyrankowski, T. Wyrobek, and O. Warren, *Nature Mat.* **5**, 697 (2006).
32. J. Deneen, W.M. Mook, A. Minor, W.W. Gerberich, and C.B. Carter, *J. Mater. Sci.* **41**, 4477 (2006).
33. J. Li, K.J.V. Vliet, T. Zhu, S. Yip, and S. Suresh, *Nature Mat.* **418**, 307 (2002).
34. J.D. Nowak, W.M. Mook, A.M. Minor, W.W. Gerberich, and C.B. Carter, *Phil. Mag.* **87,** 29 (2007).
35. M.J. Cordill, M.D. Chambers, M.S. Lund, D.M. Hallman, C.R. Perrey, C.B. Carter, A. Bapat, U. Kortshagen, and W.W. Gerberich, *Acta Mater.* **54**, 4515 (2006).
36. C.E. Carlton and P.J. Ferreira, *MRS 2005 Fall Meeting, Boston, MA* **903E**, 0903 (2005).
37. G.E. Dieter, *Mechanical Metallurgy* (New York, McGraw-Hill, 1986).
38. Y. Xiang, D.J. Srolovitz, and L.T. Cheng, *Acta Mater.* **52**, 1745 (2004).
39. Y. Xiang and D.J. Srolovitz, *Phil. Mag.* **86**, 3937 (2006).
40. B.G. Clark, I.M. Robertson, L.M. Dougherty, D.C. Ahn, and P. Sofronis, *J. Mater. Res.* **20**, 1792 (2005).
41. J. Rösler and E. Arzt, *Acta Metall. et Mater.* **38**, 671 (1990).
42. E. Arzt, G. Dehm, P. Gumbsch, O. Kraft, and D. Weiss. *Prog. Mater. Sci.* **46**, 283 (2001).
43. E.A. Marquis, D.N. Seidman, and D.C. Dunand, *Acta Mater.* **50**, 4021 (2002).
44. D.N. Seidman, C.B. Fuller, J.L. Murray, *Acta Mater.* **53**, 5401 (2005).
45. I.M. Robertson and D. Teter, *Miscrosc. Res. Tech.* **42**, 260 (1998.).
46. I.M. Robertson, *Enginr. Fract. Mech.* **68**, 671 (2001).
47. H.K. Birnbaum and P. Sofronis, *Mater. Sci. Eng. A, Struct. Mater., Prop. Microstruct. Process.* **A176**, 191 (1993).
48. J. Lufrano, P. Sofronis, and H.K. Birnbaum, *J. Mech. Phys. Solids* **44**, 179 (1996).
49. P. Sofronis and I.M. Robertson, *Phil. Mag. A* **82**, 3405 (2002).
50. Y. Liang, P. Sofronis, and N. Aravas, *Acta Mater.* **51**, 2717 (2003).
51. J. Roberto and Tomas Diaz de la Rubia, http://www.sc.doe.gov/bes/reports/files/ANES_rpt.pdf.(2006) (accessed January 2008).
52. B.D. Wirth, V.V. Bulatov, and T. De La Diaz Rubia, *J. Engr. Mater.& Techn.* **124**, 329 (2002).
53. J.S. Robach, I.M. Robertson, B.D. Wirth, and A. Arsenlis, *Phil. Mag. A* **83**, 955 (2003).
54. Y. Matsukawa, Y.N. Osetsky, R.E. Stoller, and S.J. Zinkle, *JOM* **56**, 347 (2004).
55. I.M. Robertson, A. Beaudoin, K. Al-Fadhalah, L. Chun-Ming, J. Robach, B.D. Wirth, A. Arsenlis, D. Ahn, and P. Sofronis. *Mater. Sci. & Engin. A* **400–401**, 245 (2005).
56. Y. Matsukawa, Y.N. Osetsky, R.E. Stoller, and S.J. Zinkle, *J. Nucl.Mater.* **351**, 285 (2006).
57. J.S. Robach, I.M. Robertson, H.J. Lee, B.D. Wirth, *Acta Mater.* **54**, 1679 (2006).
58. N.M. Ghoniem, S.H. Tong, J. Huang, B.N. Singh, and M. Wen, *J. Nucl.Mater.* **307–311**, 843 (2002).
59. B.N. Singh, A.J.E. Foreman, and H. Trinkaus, *J. Nucl.Mater.* **249**, 103 (1997).
60. L.Z. Sun, Ghoniem N.M., S.H. Tong, and B.N. Singh, *J. Nucl.Mater.* **283–287 pt.B**, 741 (2000).
61. A. Arsenlis, B.D. Wirth, M. Rhee, *Phil. Mag.* **84**, 3617 (2004).
62. F.M. Ross, R. Hull, D. Bahnck, J.C. Bean, L. J. Peticolas, and C.A. King, *Appl. Phys. Lett.* **62**, 1426 (1993).
63. J. Bean, L.C. Feldman, A.T. Fiory, S. Nakahara, I.K. Robinson, Ge_xSi1_{-x}/Si *Strained-Layer Superlattice Grown by Molecular Beam Epitaxy,* **2** 436 (Boston, MA, USA, 1984).
64. R. Hull, J.C. Bean, D.J. Werder, and R.E. Leibenguth. *Phys. Rev. B* **40**, 1681 (1989)
65. R. Hull, and J.C. Bean. *J. Vac. Sci .&Tech A* **7**, 2580 (1989).
66. R. Hull, J.C. Bean, and C. Buescher, *J. Appl. Phys.* **66**, 837 (1989).
67. W.A. Nix, D.B. Noble, J.F. Turlo, *Proc. Mat. Res. Soc.* **188**, 315 (1990).
68. M. Imai and K. Sumino, *Phil. Mag.* **A47**, 599. (1983).

69. B.W. Dodson and J.Y. Tsao, *Appl. Phys. Lett.* **51**, 1325 (1987).
70. R. Hull, J.C. Bean, L. Peticolas, D. Bahnck, and F. Unterwald, *J. Appl. Phys.* **70**, 2052 (1990).
71. R. Hull and J.C. Bean, *Phys. Stat. Sol. (A)* **138**, 533 (1993).
72. F. Louchet, Y. Brechet, J. Pelissier, and D.C. Muchy, *Phil. Mag. A* **57**, 327 (1988).
73. M. Inoue, K. Suzuki, H. Amasuga, Y. Mera, and K. Maeda, *J. Appl. Phys.* **83**, 1953 (1998).
74. H.R. Kolar, J.C.H. Spence, H. Alexander, *Phys. Rev. Lett.* **77**, 4031 (1996).
75. E. Orowan. *Proc. Phys. Soc.* **52**, 8 (1940).
76. D.C. Houghton, *J. Appl. Phys.* **70**, 2136 (1991).
77. D.D. Perovic and D.C. Houghton, *Proc. Mat. Res Soc.* **263**, 391 (1992).
78. E.A. Stach, K.W. Schwarz, R. Hull, F.M. Ross, and R.M. Tromp, *Phys. Rev. Lett.* **84**, 947 (2000).
79. R. Hull and J.C. Bean. *Appl. Phys. Lett.* **54**, 925 (1989).
80. L.B. Freund, *J. Appl. Phys.* **68**, 2073 (1990).
81. K.W. Schwarz, *Phys. Rev. Lett.* **78**, 4785 (1997).
82. T.J. Gosling, S.C. Jain, J.R. Willis, A. Atkinson, and R. Bullough, *Phil. Mag.* **A66**, 119 (1992).
83. W.D. Nix, *Metall. Trans. A* **20**, 2217 (1989).
84. E. Arzt, *Acta Mater.* **46**, 5611 (1998).

85. S.P. Baker, *Mater. Sci. & Engin. A* **319–321**, 16 (2001).
86. P. Wellner, O. Kraft, G. Dehm, J. Andersons, and E. Arzt, *Acta Mater.* **52**, 2325 (2004)
87. Y. Choi and S. Suresh, *Acta Mater.* **50**, 1881 (2002).
88. K.S. Kumar, S. Suresh, M.F. Chisholm, J.A. Horton, and P. Wang, *Acta Mater.* **51**, 387 (2003).
89. E. Eiper, J. Keckes, K.J. Martinschitz, I. Zizak, M. Cabie, and G. Dehm, *Acta Mater.* **55**, 1941 (2007).
90. R. Venkatraman, J.C. Bravman, W.D. Nix, P.W. Davies, P.A. Flinn, and D.B. Fraser, *J. Electron. Mater.* **19**, 1231 (1990).
91. O. Kraft, M. Hommel, and E. Arzt, *Mater. Sci. Eng. A*, **A288**, 209 (2000).
92. G. Dehm, T.J. Balk, H. Edongue, and E. Arzt, *Microelectronic Engineering* **70**, 412 (2003).
93. G. Dehm, T. Wagner, T.J. Balk, E. Arzt, and B.J. Inkson, *J. Mater Sci. and Tech.* **18**, 113 (2002).
94. B.J. Inkson, G. Dehm, and T. Wagner, *Acta Mater.* **50**, 5033 (2002).
95. G. Dehm and E. Arzt, *Appl. Phys. Lett.* **77**, 1126 (2000).
96. M. Legros, G. Dehm, T.J. Balk, E. Arzt, O. Bostrom, P. Gergaud, O. Thomas, and

B. Kaouache, *Plasticity-Related Phenomena in Metallic Films on Substrates* 63 (San Francisco, CA, Mater. Res. Soc, 2003).
97. G. Dehm, C. Motz, C. Scheu, H. Clemens, P.H. Mayrhofer, and C. Mitterer. *Advanced Engineering Materials* **8**, 1033 (2006).
98. K. Deok-kee, W.D. Nix, R.P. Vinci, M.D. Deal, and J.D. Plummer, *J. Appl. Phys.* **90**, 781 (2001).
99. H. Gao, L. Zhang, W.D. Nix, C.V. Thompson, and E. Arzt, *Acta Mater.* **47**, 2865 (1999).
100. T.J. Balk, G. Dehm, and E. Arzt, *Parallel Glide: A Fundamentally Different Type of Dislocation Motion in Ultrathin Metal Films* **779**, 87 (San Francisco, CA, Materials Research Society, 2003).
101. G. Dehm, M. Legros, and B. Heiland. *J. Mater. Sci.* **41**, 4484 (2006).
102. S.H. Oh, M. Legros, D. Kiener, P. Gruber, and G. Dehm, *Acta Mater.* **55**, 5558 (2007).
103. T.J. Balk, G. Dehm, and E. Arzt, *Acta Mater.* **51**, 4471 (2003).
104. M. Chen, E. Ma, K.J. Hemker, H. Sheng, Y. Wang, and X. Cheng. *Science* **300**, 1275 (2003).
105. K. Hattar, J.H. Han, D.M. Follstaedt, S.J. Hearne, T.A. Saif, and I.M. Robertson, *Length Scale Effects on Deformation and Failure Mechanisms of Ultra-Fine Grained Aluminum* **907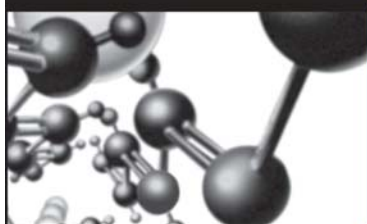**, 1 (Boston, MA, Materials Research Society, 2005). ☐